RSC Advances

PAPER

View Article Online
View Journal | View Issue

Cite this: *RSC Adv.*, 2014, **4**, 64737

Bilayered photoanode from rutile TiO_2 nanorods and hierarchical anatase TiO_2 hollow spheres: a candidate for enhanced efficiency dye sensitized solar cells

Peilu Zhao,[a] Pengfei Cheng,[b] Biao Wang,[c] Shiting Yao,[a] Peng Sun,[a] Fengmin Liu,*[a] Jie Zheng[a] and Geyu Lu*[a]

Received 7th October 2014
Accepted 18th November 2014

DOI: 10.1039/c4ra11895b

www.rsc.org/advances

A bilayered photoanode for dye-sensitized solar cells (DSSCs) was constructed with the top layer using TiO_2 hierarchical hollow spheres (THS) and the second layer based on 3D TiO_2 nanorods. The anatase THS with diameters of 400–600 nm and with a specific surface area of 100.3 $m^2\ g^{-1}$ were synthesized *via* a simple hydrothermal method. As a light scattering layer, the THS could provide dual-functions of adsorbing dye molecules and strong light-harvesting efficiency. The 3D TiO_2 nanorods consisting of 1D vertically aligned rutile TiO_2 nanorods (TNR) and 3D TiO_2 nanoflowers (TNF) were synthesized by a one-step hydrothermal method. The unique 3D nanostructure could offer a better light scattering capability, faster electron transport and lower electron recombination. Consequentially, the bilayered cell exhibited a much higher short-circuit photocurrent density of 15.60 mA cm^{-2} and energy conversion efficiency of 7.50%, which indicated a 108.6% and a 36.8% increment of cell efficiency compared to the TNR-F electrode (7.36 mA cm^{-2}, 3.60%) and THS electrode (13.20 mA cm^{-2}, 5.48%), respectively.

Introduction

Nowadays, environmental pollution and the lack of renewable energy resources have become two critical challenging issues for human beings. As the most important environmentally-friendly and renewable energy resource, solar energy plays a key role towards solving these problems. Dye sensitized solar cells (DSSCs), a viable, low cost method of producing solar electricity, is regarded as a promising candidate for the next generation solar cells and has attracted extensive interest due to simple fabrication procedures, environmental friendliness, high theoretical efficiency and good plasticity.[1–4] During the last two decades, much effort has been devoted to the development of high performance of DSSCs. In particular, nanoporous polycrystalline titania has been extensively used and made significant achievements in DSSCs due to its unique physical and chemical properties, low cost and facile preparation.[5–10] When TiO_2 is assembled in devices, the photovoltaic performance of the device is strongly influenced by the crystal structure, crystallite size[11–13] and morphology of the TiO_2 such as nanorods,[14] nanotubes,[15,16] nanowires,[17,18] nanoflowers[19] and microspheres.[20,21] Moreover, the structure of the photoanode plays an important role in enhancing the performance of cells. Our group has been interested in synthetizing TiO_2 and other semiconductor materials that apply to the DSSCs for several years.[22,23]

In order to improve the performance of DSSCs, some strategies and new methods that synthetize TiO_2 with novel morphology and design new structures for photoanode have been developed. One of the strategies is to fabricate double-layer films of nanorods and nanoparticles to increase the loading amount of dye molecules and electron transport rate of the DSSCs.[24] Although the 1D nanorods with lower surface area and lower dye loading than 0D nanoparticles, they are very suitable as under layer of the film because of fewer grain boundaries, lower transfer resistance and longer electron lifetime.[25–29] In DSSCs, the light scattering layer is very important in enhancing the power conversion efficiency, because it can increase the optical path length which irradiate into the TiO_2 film and improve the light-harvesting capacity. As is well known, small nanoparticles (10–20 nm) have larger surface areas to adsorb dye molecules but with inefficient light scattering ability and therefore result in poor light-harvesting efficiency. Hence, there will be much desire to design and synthesize a type of material as the top layer which simultaneously has a large surface area to adsorb more dye molecules and efficient light harvesting ability.

In our recent work, we fabricated DSSCs assembled using TiO_2 bilayered films as photoanodes, comprising THS light-scattering layer and 3D TNR-F under layer. This novel 1D nanorods and 3D nanoflowers of rutile TiO_2 were developed by a

[a]*EE, Jilin University, Changchun, Jilin, China. E-mail: lugy@jlu.edu.cn*
[b]*School of Aerospace Science and Technology, Xidian University, PR China*
[c]*Changchun Institute of Optics, Fine Mechanics and Physics, Changchun, China*

simple one-step hydrothermal method. The interface and transient properties of TNR-F based devices, studied by electrochemical impedance spectroscopy (EIS), showed fast electron transport and low recombination rate. The anatase THS with the size of 400–600 nm were synthesized by hydrothermal method using colloidal SiO_2 spheres as templates. Nitrogen adsorption isotherm analysis indicated that the obtained hierarchical THS had an extraordinary specific surface area which would enhance the light-harvesting capacity and dye adsorption amount. The hollow structure also exhibited excellent performance in light absorption due to the multiple reflections of light inside the THS. Moreover, the tight connection of spheres by nanosheets offered direct electrons transfer paths across adjacent spheres with less crystal boundaries, which was especially significant for application as scattering layer in porous photoanode films.[30–33] Indeed, as-prepared DSSCs had achieved much improved efficiency compared to cells fabricated with monolayered TNR-F film and THS film.

Experimental section

Materials preparation

All starting chemicals were analytical grade and used without further purification. The 3D TNR-F film grown on FTO was prepared by one-step hydrothermal method. Typically, 0.25 mL tetrabutyl titanate (TBT) was added into 10 mL mixed solution composed of 5 mL HCl (36 wt%), 4 mL deionized water and 1 mL HAc (98 wt%). After continual stirring to form a transparent solution, the mixture was injected into a 45 mL Teflon-lined autoclave. A piece of F-doped SnO_2 (FTO) glass (resistivity 14 Ω per square, Nippon Sheet Glass, Japan) ultrasonically cleaned in acetone and deionized water, respectively, for 30 min was placed in the autoclave which was then sealed and heated at 150 °C for 5 h. When the autoclave cooled to room temperature, the TiO_2 films were washed several times with distilled water and dried in an oven at 80 °C for 1 h (designated as TNR-F).

The TiO_2 hollow spheres (designated as THS) were synthesised by a hard template method. Firstly, monodisperse SiO_2 sphere templates with average diameter of 400 nm were synthesized using a modified Stöber method.[34] Then, TiO_2 was deposited on the SiO_2 sphere templates by a sol–gel method to obtain SiO_2@TiO_2 core–shell structure.[35] In order to achieve TiO_2 hollow sphere with rough shell, 0.05 g SiO_2@TiO_2 powder was added to 30 mL of 2 M NaOH aqueous solution. After ultrasonication and stirring for 5 min alternately, the mixture was injected into a 45 mL Teflon-lined autoclave. The autoclave was then sealed and heated at 100 °C for 4 h. The as-obtained white products were collected by centrifuge, washed with 0.2 M HNO_3 solution and deionized water three times, respectively. The products were then dried at 60 °C for 8 h. Finally, the TNR-F and THS were both calcined at 450 °C for 30 min with a heating rate of 2 °C min^{-1} in air.

Characterization

The crystal structure of the samples was investigated by X-ray diffraction (XRD; Rigaku TTRIII, with Cu $K\alpha_1$ radiation). The details of the morphology and microstructure were observed by filed-emission scanning electron microscopy (FESEM, JEOL JSM-7500F, operated at an acceleration voltage of 15 kV). Transmission electron microscopy (TEM) measurements were carried out on a JEOL EM-2100 microscope, using an acceleration voltage of 200 V. The specific surface was measured using the Brunauer–Emmett–Teller (BET) equation based on the nitrogen adsorption isotherm obtained with a Micromeritics Gemini VII apparatus (Surface Area and Porosity System).

Fabrication of the DSSCs

To prepare a screen-printable paste, 0.3 g of collected THS powder was dispersed in the mixture of 5 mL of ethylalcohol and 1 g of terpinol and treated with an ultrasonic bath for 60 min. The coating of the as-prepared paste onto the FTO coated with TNR-F film was done *via* the doctor blade method. After drying at 125 °C for 6 min, the resulting double-layer film was subsequently annealed at 450 °C for 30 min in air. Then, the thick film was loaded with dye by immersing it in a 0.4 mM dye solution (dye: N-719, solvent: *t*-butanol and acetonitrile mixture with volume ratio of 1 : 1) for 24 h at room temperature. Finally, the dye-sensitized TiO_2/FTO glass films were sandwiched together with the Pt-coated FTO counter electrode. The acetonitrile/valeronitrile (85/15 v/v) electrolyte containing 0.6 M 1,2-dimethyl-3-propylimidazolium iodide, 0.03 M I_2, 0.1 M guanidinium thiocyanate and 0.5 M 4-*tert*-butylpyridine (Aldrich) was injected into the space between the anode and the cathode by using a vacuum back-filled method.

Photovoltaic measurements

The current–voltage (*I–V*) characteristics of the solar cells were measured using Keithley 2400 Source Meter under illumination (AM 1.5 G, 100 mW cm^{-2}) with a solar light simulator (Newport, model: 94023A) which was calibrated with a NREL-calibrated silicon solar cell equipped with an optical filter. The active area of the DSSC utilized in the *I–V* test was ~0.25 cm^2. Diffuse-reflectance spectra of the same film samples were performed on a Perkin-Elmer UV-vis spectrophotometer (SHIMADZU 2550). Electrochemical impedance spectroscopy (EIS) was recorded at a bias potential of −0.8 V using an electrochemical workstation (Solartron SI1287).

Results and discussion

Characterization of materials

Fig. 1 displays the SEM and TEM images of the prepared TNR-F samples. Fig. 1(a) shows a top-view of the TNR-F, indicating that the diameters of the TiO_2 nanoflowers are in the range of 6–8 μm. Fig. 1(b) shows the cross-sectional SEM image of the vertically aligned 1D nanorods with about 3.7 μm length and 3D nanoflowers on the top of them. Fig. 1(c) and (d) show TEM images of a representative nanorod broken from the TNR-F anode. The inset of Fig. 1(c) is the SAED pattern of the TNR-F, which confirms the single-crystalline nature of the rutile TiO_2 nanorods. Fig. 1(d) is the HRTEM image. The clear lattice fringes are observed along its entire length. The lattice spacings

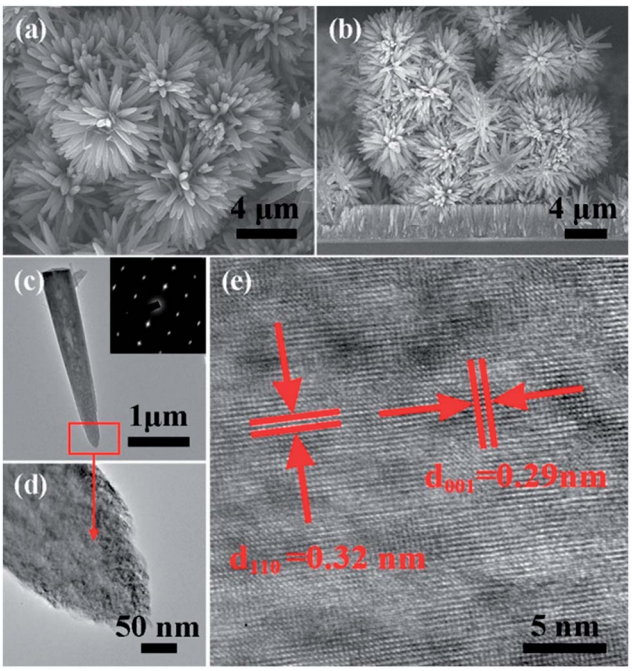

Fig. 1 (a and b) SEM images of the prepared pure TNR-F anode. (a) Top-view of the TNR-F, (b) side-view of the TNR-F. (c and d) TEM and (e) HRTEM images of a representative nanorod broken from the TNR-F anode.

of $d_{001} = 0.29$ nm and $d_{110} = 0.32$ nm imply that the 1D nanorod is growing along the $\langle 001 \rangle$ direction.

Fig. 2 displays the SEM and TEM images of the prepared THS samples. Fig. 2(a) shows the SEM image of the as-prepared THS samples. It can be seen that the TiO_2 microspheres are monodisperse and the diameter range is from 400–600 nm. The broken ones indicate the hollow structure of these microspheres. A higher magnification SEM image shown in Fig. 2(b) reveals obviously that the spherical shell is composed of serried nanosheets formed by a lot of nanoparticals. Fig. 2(c) and (d) are the TEM images of the as-prepared samples, where the hollow structure is further exhibited. The inset of Fig. 2(c) is the SAED pattern of the THS, which confirms the poly-crystalline nature of the anatase TiO_2 samples. The inter-fringe spacing parallel to the top and bottom surface is measured to be 0.38 nm, which coincides with the interlayer distance of (100) facets in anatase TiO_2, and further confirms that the TiO_2 nanosheets have a highly crystallized anatase phase structure.

The crystallinity of the hydrothermally deposited TNR-F and THS is revealed by Fig. 3(a). The diffraction peaks of the TNR-F have been indexed to the pure rutile phase (JCPDS card no. 4-551). Six distinct reflections such as (110), (101), (111), (210), (211) and (002) at 27.48°, 36.14°, 41.31°, 44.12°, 54.40° and 62.80° respectively, are clearly discernible.[36] As can be seen from the Fig. 3(a), the 2θ values at 25.28°, 37.80°,48.05°, 53.89°, 55.06°, 62.69°, 68.76°, 70.31°, and 75.03° can be assigned to (101), (004), (200), (105), (211), (204), (116), (220), and (215) crystal planes of anatase TiO_2 respectively (JCPDS card no. 21-1272). The well defined and sharp Bragg peaks with high intensity indicate good crystallinity of the THS. Meanwhile, the average crystallite size of the THS, calculated using the Scherrer formula: $D = K\lambda/\beta \cos\theta$, is about 11.2 nm. This is consistent with the information of SEM and TEM above, the N_2 adsorption–desorption isotherm, and pore size distribution of the THS.

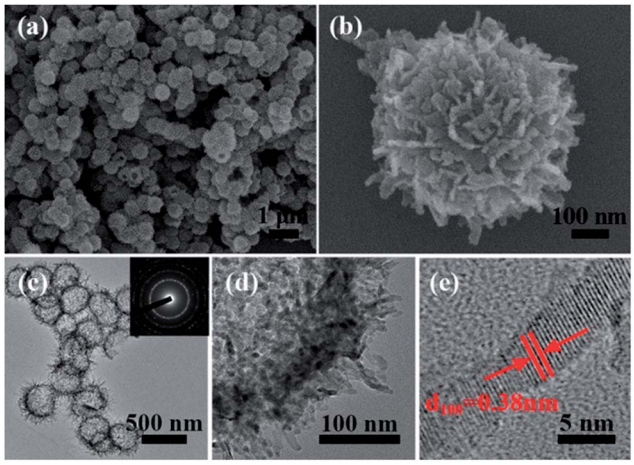

Fig. 2 (a and b) SEM images of the hierarchical THS with different magnifications. (c and d) TEM and (e) HRTEM images of as-prepared TiO_2 sphere.

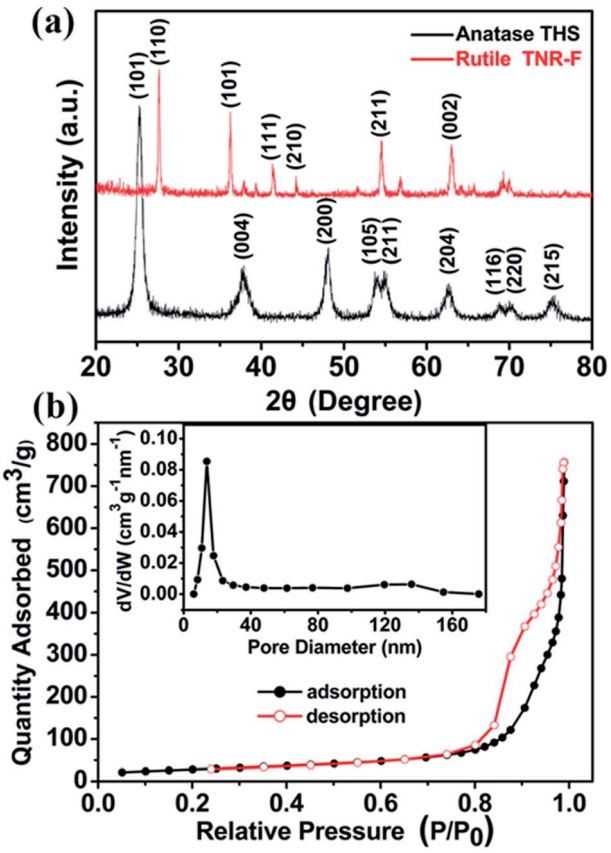

Fig. 3 (a) XRD pattern of the as-synthesized TNR-F and THS. (b) Nitrogen adsorption–desorption isotherm and the pore size distribution curve (inset) of the THS.

The N_2 adsorption–desorption isotherm exhibits typical type IV hysteresis loop, indicating the mesoporous nature of the THS (Fig. 3(b)),[37] and the rapid increase in N_2 adsorption amount at relative pressure of 1.0 illustrates that the materials contain disordered mesopores with a wide orifice, which coincides with the SEM images (Fig. 2). The approximately H3-type hysteresis loop indicates the presence of slit-like mesopores, which can also be confirmed by the pore size distribution curve. BJH pore size distribution curve calculated from the desorption branches shows an average pore size of 29.6 nm with a peak size of about 16 nm (the inset of Fig. 3(b)).[38] Moreover, The BET specific surface area of the THS is about 100.3 $m^2 g^{-1}$, much larger than the conventional P25 (50 ± 15 $m^2 g^{-1}$). This guarantees a larger amount of dye adsorption while enhancing the light harvesting of the photoanode simultaneously.

Formation mechanism

The formation mechanism of the TiO_2 hollow spheres was investigated by tracing the morphological evolution process. The formation of titanium dioxide can be briefly expressed as follows:

$$SiO_2 + 2NaOH \rightarrow Na_2SiO_3 + H_2O \quad (1)$$

$$TiO_2 + 2NaOH \rightarrow Na_2TiO_3 + H_2O \quad (2)$$

$$Na_2TiO_3 + 2HNO_3 \rightarrow 2NaNO_3 + H_2TiO_3 \quad (3)$$

$$H_2TiO_3 \rightarrow TiO_2 + H_2O \quad (4)$$

Fig. 4(a) shows the SiO_2@TiO_2 sphere which has smooth surface in the initial stage. Then, TiO_2 on the surface reacted with NaOH to form Na_2TiO_3 (reaction (2)) nanocrystallines which covered the sphere. The formation process is illustrated in Fig. 4(b)–(d). The nanocrystallized Na_2TiO_3 transformed into nanoparticals which formed serried nanosheets over the reaction time. As a result of the hydrothermal treatment, the smooth spherical shell became much rougher, which is beneficial for improving the specific surface area. Moreover, SiO_2 inside the sphere reacted with NaOH to form Na_2SiO_3 which dissolved in the solution (reaction (1)). The TiO_2 hollow sphere finally formed after the hard template was removed.

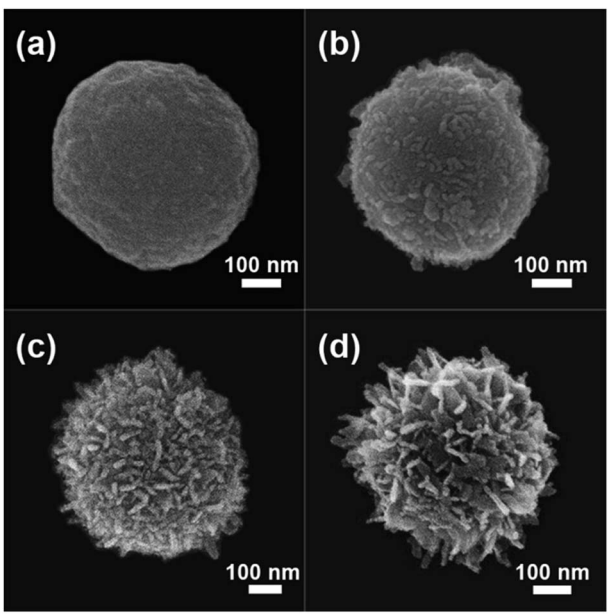

Fig. 4 Morphological evolution of the TiO_2 hollow structure: (a) 0 h; (b) 1 h; (c) 3 h; (d) 4 h.

Photovoltaic performance

The novel anatase THS with relatively large specific surface area are further used as scattering material in DSSCs. The submicron size of THS approaches to the wavelength of visible light, so the calcinated samples possess enhanced scattering effect for visible light. The bottom layer on the FTO is the TNR-F which is expected to provide fewer grain boundaries and lower transfer resistance. For comparison, Three kinds of films (film 1: TNR-F; film 2: THS; film 3: TNR-F + THS) were prepared to investigate the scattering effect and electron transport in this study. Two monolayered films prepared from TNR-F and THS with the thickness of about 16 μm and 24 μm, respectively. Film 3 (TNR-F + THS) constructed by 8 μm of THS and 16 μm of TNR-F. The schematic structure diagram of film 3 is shown in Scheme 1. Among the three photoanodes, the TNR-F + THS provides much more scattering centers and much longer light travelling distance, which leads to the apparently higher scattering effect, so the higher reflectance than the other two monolayered photoanodes is reasonable.

Fig. 5 shows the photocurrent density photovoltage (J–V) curves of the three cells, and the specific photovoltaic parameters are summarized in Table 1. Compared to film 1 (7.36 mA cm^{-2}, 0.72 V) and film 2 (13.20 mA cm^{-2}, 0.64 V), film 3 exhibits a higher short-circuit current density (15.60 mA cm^{-2}) and a higher open-circuit photovoltage (0.73 V), leading to the power conversion efficiency (η) improving from 3.60% (film 1) to 5.48% (film 2) to 7.50% (film 3). Furthermore, film 1 is thinner than film 2, but the fill factor (FF) and the open-circuit voltage (V_{oc}) of film 1 is higher, which is ascribed to faster electron transport and lower electron recombination of the 1D nanorods. Although the film 2 has the

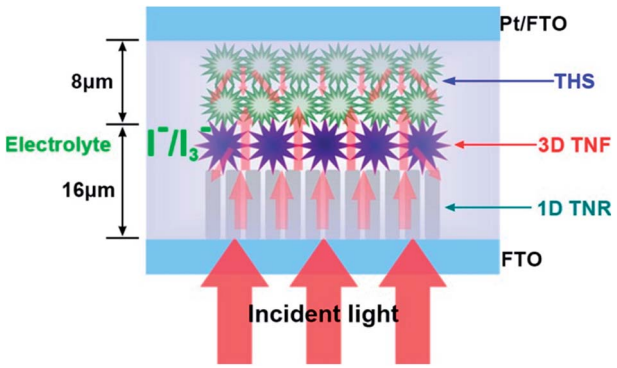

Scheme 1 Schematic diagram of cell 3 constructed by TNR-F and THS.

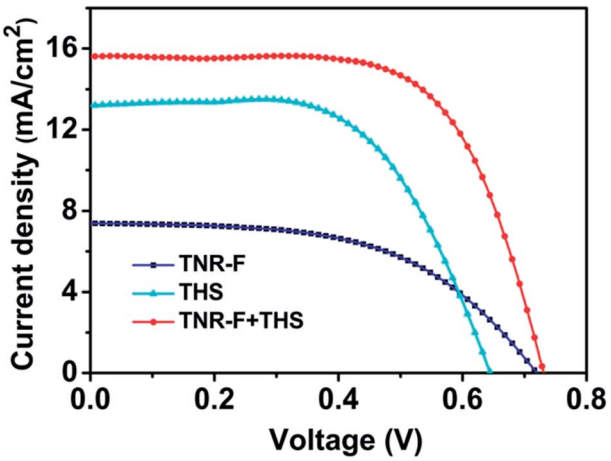

Fig. 5 J–V curves of the DSSCs based on three different photoanodes measured under one sun illumination (AM 1.5 G, 100 mW cm^{-2}).

highest dye adsorption amount, the lowest V_{oc} (0.64 V) and the relatively lower FF (0.65) restricts the photoelectric properties, leading to a 26.9% decrement of η (5.48%) compared with the film 3. It is noteworthy that the film 3 coated by the additional THS layer exhibits higher J_{sc} and V_{oc} than film 1, which means that the THS layer enhanced photovoltaic performance indeed.

It is well-known that the photocurrent of TiO_2 photoanode is strongly related to its light-harvesting capability. As a harvester of the photon, the amount of dye adsorbed has a direct effect on the light-harvesting capability of TiO_2 photoanode.[39] Therefore, to promote dye loading and light scattering of the electrodes are two equally important tasks for light-harvesting. The dye adsorption capacity of the three films was estimated *via* measuring the UV-vis absorption spectra of the solutions obtained by thorough desorption in 1 mM NaOH solution. The dye loading of film 3 is 4.3 times higher than that of film 1 and slightly lower than that of film 2 (Table 1). The higher dye adsorption capacity of film 2 is ascribed to the larger specific surface area of THS.

The UV-vis reflectivity spectrum of each film was measured to further study the light scattering property of the three films, Fig. 6(a) shows the diffuse reflectance spectra of the three bare electrode films without dye loading. These films all have high reflectivity in the wavelength range of 400–800 nm. Moreover, the TNR-F + THS film exhibits the strongest scattering effect, because the particle size of the THS is analogous to the wavelength of visible light, which can lead to a strong scattering effect according to Mie theory. Furthermore, the relatively

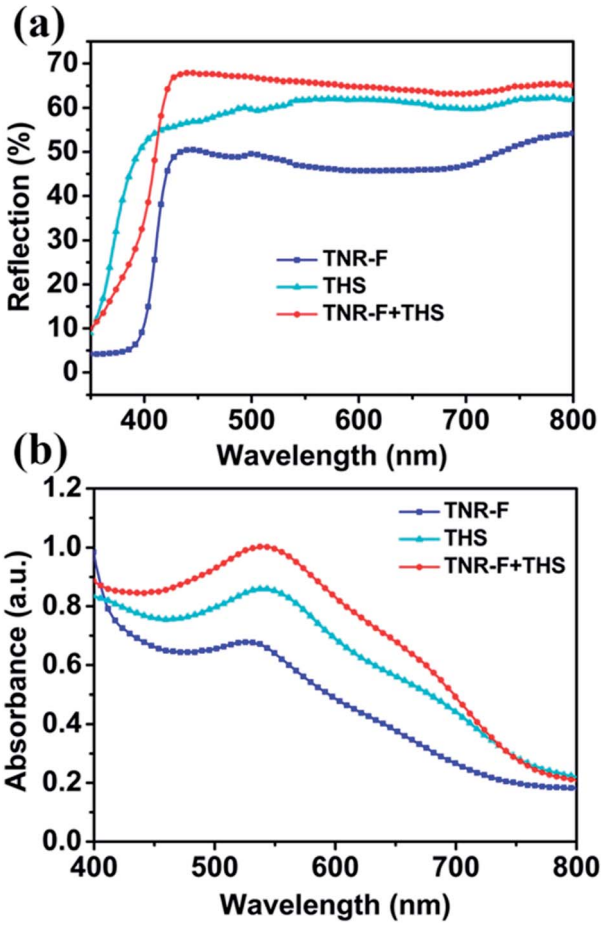

Fig. 6 (a) Diffuse reflectance spectra of the photoanode films before the dye uptaking process. (b) Absorption spectra of the photoanode films after the dye uptaking process.

higher refractive index of rutile TiO_2 (2.75) than the anatase counterpart (2.52) also contributes to an enhanced light reflectance, which can explain that the TNR-F + THS film has a better scattering effect than the THS film. After dye adsorption, UV-vis absorption spectra of the three films were measured to provide further information about light harvesting. As shown in Fig. 6(b), the TNR-F + THS film exhibits the strongest absorption intensity, implying an effective utilization rate of the incident light.

Fig. 7 shows the incident photon to current efficiency (IPCE) spectra for the three kinds of DSSCs. It can be observed that for all of the DSSCs, the maxima of the IPCE spectra appear at 525 nm (the peak of the N719 adsorption spectrum). As shown in

Table 1 Average photovoltaic data of three different photoanodes, measured under one sun illumination (AM 1.5 G 100 mW cm^{-2}) and simulative value of resistance (R_1, R_2, and R_3) from EIS spectra calculated by equivalent circuit as shown in Fig. 6

DSSC	J_{sc} (mA cm^{-2})	V_{oc} (V)	FF (%)	η (%)	R_1 (Ω)	R_2 (Ω)	R_3(Ω)	Dye adsorbed ($\times 10^{-7}$ mol cm^{-2})
TNR-F	7.36	0.72	68	3.60	31.2	8.4	21.4	0.32
THS	13.20	0.64	64	5.48	33.4	8.5	102.2	1.97
TNR-F + THS	15.60	0.73	66	7.50	31.0	8.0	23.8	1.36

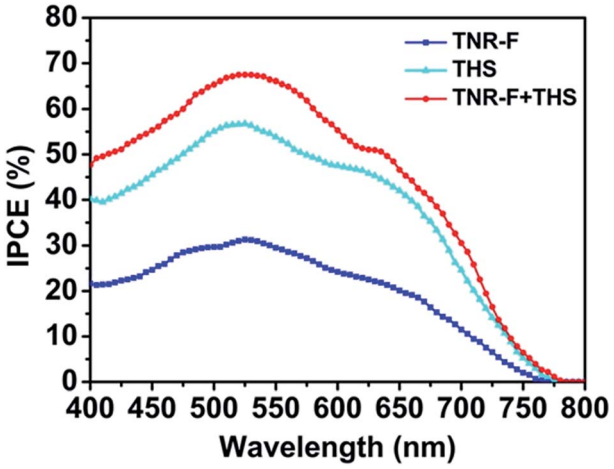

Fig. 7 IPCE spectra of the three DSSCs with TNR-F, THS and TNR-F + THS photoanodes.

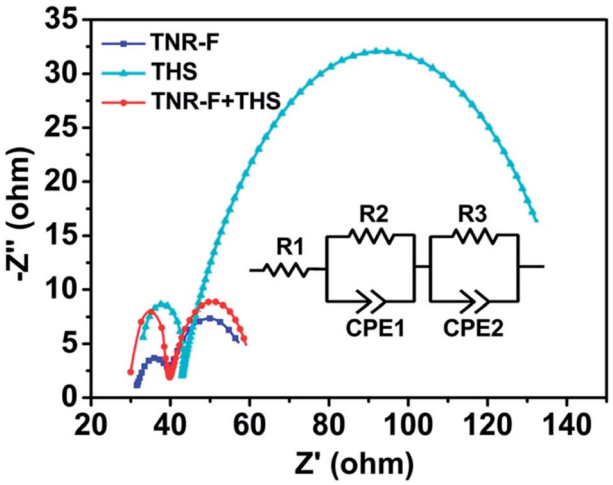

Fig. 8 Nyquist plots from electrochemical impedance spectra of the three films together measured at −0.8 V bias. The inset illustrates the equivalent circuit simulated to fit the impedance spectra.

Fig. 7, the IPCE of cell TNR-F is found to be the lowest, which is in good accordance with the *J–V* measurement and dye uptake. Compared to cell TNR-F, the IPCE of cell THS increased from 31% to 56% at around 525 nm, which can be ascribed to the relatively superior specific surface area, enabling the uniform distribution of dye molecules on the surface of the THS. Of the tested cells, cell TNR-F + THS reveals the highest IPCE values over the whole spectral region. Two main characteristics contribute to the IPCE enhancement. First, the better light-scattering ability and superior dye adsorption capacity of the top layer improve the collection of photons.[40,41] Second, the bottom layer of TNR-F provides fast electron transport, which also helps the collection of photoelectrons. The result also shows that the PCE enhancement is ascribed to the better collection of photons due to the scattering of light.

In order to investigate the charge transport and recombination in the three photoanodes, electrochemical impedance spectroscopy (EIS) was performed at a bias voltage of −0.8 V, and the frequency range was from 0.1 Hz to 10^6 Hz.[42,43] As shown in Fig. 8, Nyquist plots of all the cells demonstrate two well-defined semicircles. The larger semi-circle at intermediate frequency is attributed to charge transfer resistance at the TiO_2–dye–electrolyte interface (R_3),[44,45] which is vital for the photovoltaic performance. The smaller semi-circle at high frequency is attributed to charge transfer resistance at the electrolyte–Pt–FTO interface (R_2). R_1 represents the lumped series resistance for the transport in FTO and all the corresponding resistances outside of the cell. The inset illustrates the equivalent circuit simulated to fit the impedance spectra and the specific impedance data can be observed in Table 1. The three cells reveal similar R_1 and R_2 values due to the use of the same counter electrode (Pt/FTO glass) and electrolyte. However, compared with the cell assembled with the THS anode, the cells assembled with the TNR-F and TNR-F + THS anodes show significant reduction on R_3, which means that the 3D TNR-F makes the electron transfer easier at the TiO_2–dye–electrolyte.[46] This observation is in agreement with the lower fill factor of the THS based cell (0.64). In spite of the larger surface area, the THS can provide a large number of surface states and a longer electron transport distance in the film which leads to more recombination centres and a non-uniform FTO/TiO_2 interface. But in the TNR-F + THS based cell, the 3D nanoflowers and 1D nanorods would provide excellent electron percolation pathways for charge transfer.[47]

Conclusions

In conclusion, we have successfully synthesized 3D TNR-F photoelectrode for effective light harvesting and electron transport using a surfactant free single step hydrothermal route. We also achieved a novel hierarchical TiO_2 hollow sphere through a simple hydrothermal synthesis. A bilayered photoanode for dye-sensitized solar cells (DSSCs) was constructed using TNR-F as the bottom layer and THS as the top layer, high adsorption ability to the dye, light scattering ability, and high electron transport rate coexistence. The DSSCs based on the photoanode with a bistratal structure exhibited a much higher short-circuit photocurrent density of 15.60 mA cm^{-2} and energy conversion efficiency of 7.50%, which exhibited a 108.6% and a 36.8% increment of cell efficiency compared to those of TNR-F electrode (7.36 mA cm^{-2}, 3.60%), and those of THS electrode (13.20 mA cm^{-2}, 5.48%), respectively. The great improvements of photocurrent density and energy conversion efficiency for the bilayered cell were mainly attributed to larger amount of dye adsorption, a stronger light scattering ability, and higher electron transport rate. We consider that this facile structured route would have good potential for application in DSSCs.

Acknowledgements

This work was supported by NSFC (60906036, 61134010 and 61327804) and Program for Chang Jiang Scholars and Innovative Research Team in University (no. IRT13018), National High-Tech Research and Development Program of China (863

Program, no. 2013AA030902) and the project development plan of science and technology of Jilin Province (20130521009JH).

Notes and references

1 B. Oregan and M. Grätzel, *Nature*, 1991, **353**, 737.
2 H. J. Koo, Y. J. Kim, Y. H. Lee, W. I. Lee, K. Kim and N. G. Park, *Adv. Mater.*, 2008, **20**, 195.
3 A. Hagfeldt, G. Boschloo, L. C. Sun, L. Kloo and H. Pettersson, *Chem. Rev.*, 2010, **110**, 6595.
4 X. K. Xin, M. He, W. Han, J. Jung and Z. Q. Lin, *Angew. Chem., Int. Ed.*, 2011, **50**, 11739.
5 J. Z. Chen, L. Yang and Y. F. Tang, *J. Power Sources*, 2010, **195**, 6893.
6 N. Huang, Y. Xie, B. Sebo, Y. Liu, X. H. Sun, T. Peng, W. W. Sun, C. H. Bu, S. H. Guo and X. Z. Zhao, *J. Power Sources*, 2013, **242**, 848.
7 Y. C. Rui, Y. G. Li, Q. H. Zhang and H. Z. Wang, *Nanoscale*, 2013, **5**, 12574.
8 Z. D. Li, Y. Zhou, T. Yu, J. G. Liu and Z. G. Zou, *CrystEngComm*, 2012, **14**, 6462.
9 X. Cai, H. G. Wu, S. C. Hou, M. Peng, X. Yu and D. C. Zou, *ChemSusChem*, 2014, **7**, 474.
10 Y. P. Liu, S. R. Wang, Z. Q. Shan, X. G. Li, J. H. Tian, Y. M. Mei, H. M. Ma and K. L. Zhu, *Electrochim. Acta*, 2012, **60**, 422.
11 N. G. Park, J. van de Lagemaat and A. J. Frank, *J. Phys. Chem. B*, 2000, **104**, 8989.
12 J. Y. Liao, J. W. He, H. Xu, D. B. Kuang and C. Y. Su, *J. Mater. Chem.*, 2012, **22**, 7910.
13 J. G. Yu, J. J. Fan and L. Zhao, *Electrochim. Acta*, 2010, **55**, 597.
14 Q. L. Huang, G. Zhou, L. Fang, L. P. Hu and Z. S. Wang, *Energy Environ. Sci.*, 2011, **4**, 2145.
15 D. Gong, C. A. Grimes, O. K. Varghese, W. Hu, R. S. Singh, Z. Chen and E. C. Dickey, *J. Mater. Res.*, 2001, **16**, 3331.
16 D. X. Liu and M. Z. Yates, *Langmuir*, 2007, **23**, 10333.
17 W. Q. Wu, J. Y. Liao, H. Y. Chen, X. Y. Yu, C. Y. Su and D. B. Kuang, *J. Mater. Chem.*, 2012, **22**, 18057.
18 J. Y. Liao, B. X. Lei, H. Y. Chen, D. B. Kuang and C. Y. Su, *Energy Environ. Sci.*, 2012, **5**, 5750.
19 X. H. Tan, P. F. Qiang, D. D. Zhang, X. Cai, S. Z. Tan, P. Y. Liu and W. J. Mai, *CrystEngComm*, 2014, **16**, 1020.
20 H. Pan, J. S. Qian, Y. M. Cui, H. X. Xie and X. F. Zhou, *J. Mater. Chem.*, 2012, **22**, 6002.
21 Z. Y. Gao, Z. L. Wu, X. M. Li, J. L. Chang, D. P. Wu, P. F. Ma, F. Xu, S. Y. Gao and K. Jiang, *CrystEngComm*, 2013, **15**, 3351.
22 P. F. Cheng, S. S. Du, Y. X. Cai, F. M. Liu, P. Sun, J. Zheng and G. Y. Lu, *J. Phys. Chem. C*, 2013, **117**, 24150.
23 P. F. Cheng, Y. X. Cai, S. S. Du, P. Sun, G. Y. Lu, J. Zheng and F. M. Liu, *RSC Adv.*, 2013, **3**, 23389.
24 A. M. Bakhshayesh, M. R. Mohammadi and D. J. Fray, *Electrochim. Acta*, 2012, **78**, 384.
25 W. Ho, J. C. Yu and J. Yu, *Langmuir*, 2005, **21**, 3486.
26 H. P. Wu, L. L. Li, C. C. Chen and E. W. G. Diau, *Ceram. Int.*, 2012, **38**, 6253.
27 S. Nejati and K. K. S. Lau, *Nano Lett.*, 2010, **11**, 419.
28 C. Y. Huang, Y. C. Hsu, J. G. Chen, V. Suryanarayanan, K. M. Lee and K. C. Ho, *Sol. Energy Mater. Sol. Cells*, 2006, **90**, 2391.
29 P. Qiang, Z. Chen, P. Yang, X. Cai, S. Tan, P. Liu and W. Mai, *Nanotechnology*, 2013, **24**, 435403.
30 H. J. Koo, Y. J. Kim, Y. H. Lee, W. I. Lee, K. Kim and N. G. Park, *Adv. Mater.*, 2008, **20**, 195.
31 Y. C. Qiu, W. Chen and S. H. Yang, *Angew. Chem., Int. Ed.*, 2010, **49**, 3675.
32 K. Y. Yan, Y. C. Qiu, W. Chen, M. Zhang and S. H. Yang, *Energy Environ. Sci.*, 2011, **4**, 2168.
33 P. N. Zhu, A. S. Nair, S. R. Yang, S. J. Peng and S. Ramakrishna, *J. Mater. Chem.*, 2011, **21**, 12210.
34 Z. W. Zhang, Y. M. Zhou, Y. W. Zhang, X. L. Sheng, S. J. Zhou and S. M. Xiang, *Appl. Surf. Sci.*, 2013, **286**, 344.
35 H. L. Shen, H. H. Hu, D. Y. Liang, H. L. Meng, P. G. Li, W. H. Tang and C. Cui, *J. Alloys Compd.*, 2012, **542**, 32.
36 E. Hosono, S. Fujihara, K. Kakiuchi and H. Imai, *J. Am. Chem. Soc.*, 2004, **126**, 7790.
37 Z. Y. Gao, Z. L. Wu, X. M. Li, J. L. Chang, D. P. Wu, P. F. Ma, F. Xu, S. Y. Gao and K. Jiang, *CrystEngComm*, 2013, **15**, 3351.
38 Y. C. Rui, Y. G. Li, Q. H. Zhang and H. Z. Wang, *CrystEngComm*, 2013, **15**, 1651.
39 F. Shao, J. Sun, L. Gao, S. W. Yang and J. Q. Luo, *J. Mater. Chem.*, 2012, **22**, 6824.
40 A. Usami, *Chem. Phys. Lett.*, 1997, **277**, 105.
41 D. Colonna, S. Colodrero, H. Lindström, A. D. Carlo and H. Míguez, *Energy Environ. Sci.*, 2012, **5**, 8238.
42 R. Kern, R. Sastrawan, J. Ferber, R. Stangl and J. Luther, *Electrochim. Acta*, 2002, **47**, 4213.
43 J. Qian, P. Liu, Y. Xiao, Y. Jiang, Y. Cao, X. Ai and H. Yang, *Adv. Mater.*, 2009, **21**, 3663.
44 Q. Wang, J. E. Moser and M. Grätzel, *J. Phys. Chem. B*, 2005, **109**, 14945.
45 R. Buonsanti, E. Carlino, C. Giannini, D. Altamura, L. D. Marco, R. Giannuzzi, M. Manca, G. Gigli and P. D. Cozzoli, *J. Am. Chem. Soc.*, 2011, **133**, 19216.
46 F. J. Knorr, D. Zhang and J. L. McHale, *Langmuir*, 2007, **23**, 8686.
47 Q. Wang, S. Ito, M. Grätzel, F. Fabregat-Santiago, I. Mora-Seró, J. Bisquert, T. Bessho and H. Imai, *J. Phys. Chem. B*, 2006, **110**, 25210.